Journal Pre-proof
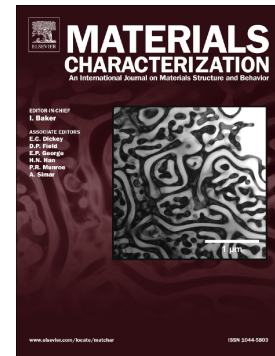
Multiscale characterization of the nucleation and 3D structure of Al3Sc phases using electron microscopy and synchrotron X-ray tomography

Yuliang Zhao, Weiwen Zhang, Billy Koe, Wenjia Du, Mengmeng Wang, Weilin Wang, Elodie Boller, Alexander Rack, Zhenzhong Sun, Da Shu, Baode Sun, Jiawei Mi

Please cite this article as: Y. Zhao, W. Zhang, B. Koe, et al., Multiscale characterization of the nucleation and 3D structure of Al3Sc phases using electron microscopy and synchrotron X-ray tomography, *Materials Characterization* (2020), https://doi.org/10.1016/j.matchar.2020.110353

This is a PDF file of an article that has undergone enhancements after acceptance, such as the addition of a cover page and metadata, and formatting for readability, but it is not yet the definitive version of record. This version will undergo additional copyediting, typesetting and review before it is published in its final form, but we are providing this version to give early visibility of the article. Please note that, during the production process, errors may be discovered which could affect the content, and all legal disclaimers that apply to the journal pertain.

Multiscale characterization of the nucleation and 3D structure of Al₃Sc phases using electron microscopy and synchrotron X-ray tomography

Yuliang Zhao [a, b], Weiwen Zhang [b*], Billy Koe [c, d], Wenjia Du [c], Mengmeng Wang [e], Weilin Wang [e], Elodie Boller [f], Alexander Rack [f], Zhenzhong Sun [a], Da Shu [e], Baode Sun [e], Jiawei Mi [c, e**]

[a] Neutron Scattering Technical Engineering Research Centre, School of Mechanical Engineering, Dongguan University of Technology, Dongguan, 523808, P.R. China

[b] National Engineering Research Centre of Near-net-shape Forming for Metallic Materials, South China University of Technology, Guangzhou, 510641, P.R. China

[c] Department of Engineering, University of Hull, East Yorkshire, HU6 7RX, UK

[d] Diamond Light Source, Harwell Science & Innovation Campus, Oxfordshire, OX11 0DE, UK

[e] Shanghai Key Laboratory of Advanced High-Temperature Materials and Precision Forming, School of Materials Science and Engineering, Shanghai Jiao Tong University, Shanghai, 200240, P.R. China

[f] ESRF-The European Synchrotron, 71 Avenue des Martyrs, 38000 Grenoble, France

Corresponding author: mewzhang@scut.edu.cn (W. Zhang); J.Mi@hull.ac.uk (J. Mi)

Abstract

Scandium (Sc) has been long recognized as one of the most effective grain refining elements for Al alloys because of the Al₃Sc phases formed in an Al melt containing Sc. However, there are still lack of comprehensive studies on the exact mechanism of how Al₃Sc phases are nucleated in Al melt and their true 3D structures.

1

In this paper, we used scanning/transmission electron microscopy and synchrotron X-ray tomography to study the nucleation and true 3D structure of primary Al_3Sc phases in an Al-2wt.%Sc alloy. The multiscale characterization approach revealed that the micrometre α-Al_2O_3 particles present in the Al melt can facilitate the formation of stacking faults at the α-Al_2O_3/Al_3Sc interface and therefore promote heterogenous nucleation of Al_3Sc phases. SEM and tomography clearly revealed that individual primary Al_3Sc phases were simple cubes with the edge length of 10~35 μm; and majority of them were interconnected to form clusters with the peak value of 10000 μm^3. At the interface between an Al matrix and an Al_3Sc cube, the Al_3Sc phases can also grow into nanometre size particle clusters due to the depletion of Sc.

Keywords: Multiscale characterisation; Al_3Sc intermetallics; Al alloy; Electron microscopy; Synchrotron X-ray tomography

1. Introduction

Aluminium (Al) alloys are the most widely used light-weight metal alloys in the world, especially in packaging, building and transportation industry [1]. In most load-bearing structural applications, it is often desirable for Al alloys to have a good combination of high strength and high ductility. The common industrial practice to achieve this in the solidification processes is by refining the grain structures of Al alloys by either adding external grain refiners [2, 3] or by applying external fields [4]. It has been long recognized that, among all the elements or materials used as Al grain refiners, Scandium (Sc) is the most effective grain refiner element. Sc has the combined beneficial effects on (1) grain refining; (2) precipitation strengthening, and (3) recrystallization enhancing [5-9]. The common practice of adding Sc into an Al

melt is through an Al-Sc master alloy (Al-2%wtSc is the commonly used master alloy) in which $L1_2$ type Al_3Sc primary phases (with a very similar crystal lattice, about 1.34% to that of α-Al [8]) are formed and they act as heterogeneous nucleation sites for α-Al grains [10-12]. Other elements, for example, Zr can be also used to partially replace Sc to form $Al_3(ScZr)$ type phases, which have core-shell type structure with high strength and excellent thermal-stability [13, 14]. In addition, the cost of Sc is very high, using other elements with similar grain refining performance to replace Sc can reduce cost effectively [15-18].

The size, 3D structures (morphology) and spatial distribution of Al_3Sc phases are important factors in determining their grain refinement performance in Al alloys [10, 19]; and any undesired agglomeration in the Al alloy melt could lead to the reduction in refinement efficiency [20]. Previous studies on the structures (morphology) of Al_3Sc phases were normally carried out using conventional electron microscopy. Such techniques are not able to reveal the true 3D morphology and distribution due to the nature of just observing 2D sections of the samples. For example, Li *et al.* [17] suggested that 3D morphology of $Al_3(ScZr)$ particles are near-globular structures and located within the α-Al matrix or grain boundary; while Kastner *et al.* [21] argued that primary $Al_3(ScZr)$ particles exhibited equiaxed shapes. Hence, a full and quantitative understanding on the particle size, morphology and spatial distribution in 3D is essential for developing strategies to improve the grain refinement performance of Al_3Sc phases. In recent years, high-brilliance synchrotron X-ray has been widely used in obtaining 3D information for phases (particles) of size above ~ 1 μm [22]. However, so far, there is very limited report on true 3D characterisation of primary Al_3Sc phases in Al alloys by synchrotron X-ray tomography.

In the present work, we used synchrotron X-ray tomography to quantify the size, 3D morphology and spatial distribution of the primary Al_3Sc phases in an Al-2%Sc alloy. We also used scanning/transmission electron microscopy (SEM/TEM) plus electron backscattered diffraction method to study the nucleation sites for the primary Al_3Sc phases and the characteristics of the stacking faults across the interface between the aluminium oxides and Al_3Sc cubes; and the morphology of nanometre size Al_3Sc phases across the interface of aluminium matrix and Al_3Sc cubes.

2. Alloys, equipment and characterization methods

2.1 Deep-etching of samples and SEM analysis

An Al-2.0%Sc (wt.%) master alloy was used in this study. For 2D microstructural characterisation, a Nova SEM 430 (FEI, Thermo Fisher Scientific, USA, with field emission gun) coupled with an energy-dispersive spectrometer (EDS) and EBSD detector was used. The working voltage used was 20 kV. The samples were deeply-etched to partially remove the Al matrix and expose the Al_3Sc phases using a mixture of high-purity iodine and methanol solution (10 g iodine per 100 mL methanol for 4 hours) [23]. The etched samples were ultrasonic cleaning for 10 min in an anhydrous ethanol solution. The primary Al_3Sc particles were then examined carefully by SEM and EDS with a focus on finding the possible nucleation sites.

2.2 EBSD analysis

The samples for EBSD measurement were polished using an Ion Beam Milling machine (Leica EM TIC 3, Germany) operated at 5 kV for 1 hour, and then 3 kV for 0.5 hour. In EBSD measurement, the sample to detector distance was set to ~10 mm, and the sample was tilted 70° with respect to the detector (HKL Channel 5, Oxford

Instruments, UK). The pattern binning was 2 × 2, and 37 EBSD patterns were collected every second (0.027 second per pattern). The voltage used was 20 kV and the magnification were from 500 to 2000. The scanning step size was set at 0.5 µm and the total scanning time was between 2 and 4 hours depending on the scanning areas. Primary Al_3Sc phase and α-Al matrix have very similar crystal structure, it is difficult to distinguish the two phases by using Kikuchi patterns only. Hence, we used the true phase model embedded in the HKL channel 5 to distinguish the two phases.

2.3 Focus ion beam milling of thin foils and TEM analysis

The thin foil samples for TEM analysis were also machined by using the same Ion Beam Milling machine with the voltage operated at 5 kV. Fig. 1 shows images of the machining steps. A sub-micrometre feature (a possible nucleation site for the Al_3Sc phases) was first identified at the centre of a blocky Al_3Sc phase (Fig. 1a). Secondly, a thin slice of ~1 µm thick was cut on the surface by ion beam (Fig. 1b). Thirdly, a trench was milled around the thin slice (Fig. 1c). The thin slice was lifted out the trench, and then welded onto a sample holder (Fig. 1d). Finally, the thin slice was further ion milled to about 70-80 nm thick (the cross section in SEM was directly measured) and then transferred to a JEOL 2100F STEM for observation. The SEM-EDS line scan (Fig. 1e, f) across the initially identified feature confirmed that the feature is an aluminium oxide particle.

2.4 Synchrotron X-ray tomography

The synchrotron X-ray tomography experiment was carried out at beamline ID 19 of the European Synchrotron Radiation Facility (ESRF), France. The samples were machined into ~1 mm diameter rod, and the detailed sample preparation procedure can be found in [24-27]. The parameters used for the tomography acquisition were

5

summarized in Table 1. The standard filtered-back projection was used for tomographic reconstructions via an in-house developed software package, PyHST2 [28]. The PyHST2 software is highly optimised for speed and data throughput using the ESRF-specific computing infrastructure. Fig. 2 shows the image processing procedure and method employed for 3D microstructure segmentation and rendering. ImageJ (Version 1.52a) [29] was used to enhance the contrast between the primary Al_3Sc phases and Al matrix (Fig. 2b). The 3D bilateral filter and Avizo Lite v9.0.1 (Thermo Fish Scientific) [30] were used for segmentation and volume rendering (Fig. 2c, d). A volume of 200^3 voxels was selected to show the 3D structure and distribution of primary Al_3Sc phases (Fig. 2e).

The mean curvature H and Gaussian curvature K [31] were used to characterize the surface curvature:

$$H = 0.5 * \left(\frac{1}{R_1} + \frac{1}{R_2} \right) \tag{1}$$

$$K = \left(\frac{1}{R_1 * R_2} \right) \tag{2}$$

where R_1 and R_2 are the two principal curvatures at an arbitrary point on a surface, respectively. The equivalent diameter D_{eq} and specific surface area (SSA) were also used to characterize the 3D morphology of primary Al_3Sc phases. The equivalent diameter is an approximate method to calculate the diameter of an arbitrary shape with a volume of V [32]:

$$D_{eq} = \sqrt[3]{\frac{6V}{\pi}} \tag{3}$$

3. Results and Discussion

Fig. 3 shows that, in 2D, most of the primary Al_3Sc phases (the grey phases) exhibit quadrilateral or triangular shapes. Fig. 4 shows the EBSD analysis of the

6

Al_3Sc phases. Due to the very similar crystal structure between Al and Al_3Sc (their mismatch in lattice parameter is only 1.34% [8]), it was impossible to differentiate the two phases by only indexing the Kikuchi patterns (see Fig. 4c and d). The true phase model embedded in the HKL channel 5 was used to identify the two phases (see Fig. 4b, yellow for the Al_3Sc phase, pink for the Al matrix). Fig. 4e shows the grain size of the Al-2Sc master alloy obtained from the EBSD inverse pole figure. Crystal orientation of the Al_3Sc phases is very similar to that of the α-Al phases around the Al_3Sc [10-12]. The α-Al grains are shown in Fig. 4f. The inserted graph shows their grain size distribution, ranging from 20 to 60 μm with the average grain size of 41.60 μm.

Fig. 5a shows the FIB machined thin foil. Region A (containing an interface between the Al matrix and Al_3Sc phase), and region B (containing an aluminium oxide "embedded in" the Al_3Sc phase) were further studied by TEM. On the Al side near the Al-Al_3Sc interface, many small round particles (with diameters in the range of 20-80 nm) were found. EDS (Fig. 5c, d) element mapping confirmed that they are indeed smaller Al_3Sc particles. Fig. 6 shows high resolution images of the Al-Al_3Sc interface. Fig. 6b further confirm that these tiny Al_3Sc particles have the same crystal structure as the primary Al_3Sc particle. The line scanning (Fig. 6c and d) shows that the change of Sc concentration across the interface, which is formed through solute diffusion at the later stage of solidification.

According to the Al-Sc binary phase diagram (at the Al-rich corner) [8, 33], at 780 °C, the solubility of Al_3Sc in Al melt is 2.0 wt.%, but reduced to 0.5 wt.% at 659 °C. During the solidification of the Al-2%Sc alloy melt (until the eutectic temperature, i.e. 659 °C), primary Al_3Sc phases formed and grew continuously. Sc has low diffusion rate in Al at the temperature near the eutectic point (for example,

1.02×10^{-13} m^2/s at 659 °C calculated by the diffusion coefficient equation reported in [34]), the rate of Sc atom diffusion through the Al matrix does not match the growth rate of the primary Sc phases, creating a Sc depletion layer at the Al-Al$_3$Sc interface as evidenced by the images showed in Fig. 5b, c, d. Such Sc depletion layer prevented further growth of the existing primary Al$_3$Sc phase on one side, and nucleated many tiny Al$_3$Sc particles on the other side as clearly showed by Fig. 5b, c, d. Such segregation behaviour of Al$_3$Sc phases was also reported in [35, 36]. These tiny Al$_3$Sc particles are nucleated from the solidification process. They are not the primary phases. They are formed via solute diffusion at the later stage of solidification.

Fig. 7 shows the High-Angle Annular Dark Field (HADDF)-STEM images of the interfacial region between the Al$_3$Sc phase and an oxide. EDS elemental mapping of the interfacial region (Figs. 7b, c, d) indicated that oxygen was present on both phases (those on the Al$_3$Sc were possibly due to oxidization during sample preparation). The SDAP image (Fig. 7f) confirmed that the crystal structure of the oxide is α-Al$_2$O$_3$ (rhombohedral structure with the lattice parameters a = 0.4782 nm, c = 1.3057 nm). Furthermore, high density of stacking faults was found on the Al$_3$Sc phase (Fig. 7e) near the Al$_3$Sc-Al$_2$O$_3$ interface. Fig. 7f shows the high-resolution image of a stacking fault marked in Fig. 7e by dash red rectangle. These discontinuous stacking faults are relatively short because of the high stacking faults energy. Usually, discontinuous stacking faults in an Al alloys inhibits the movement of dislocation and therefore improve strength [37]. Such evidence indicated that although α-Al$_2$O$_3$ may be not the "energy favourite" site for nucleating Al$_3$Sc directly. But, the presence of α-Al$_2$O$_3$ in the Al-2wt. Sc% melt (which is common for all Al alloy melt) facilitated the formation of a large number of stacking faults at the vicinity of the

8

Al_2O_3-Al_3Sc interface. These stacking faults at the Al_2O_3-Al_3Sc interface have lower energy compared to the formation of large grain boundaries [38-39]. Hence, they promote the nucleation of Al_3Sc phases [40], rather than Al gains.

Fig. 8 shows the structures and morphologies of the Al_3Sc phases in 3D, and some statistical analysis results (Fig. 8d, e). Both tomography and deeply-etched SEM observation indicate that the Al_3Sc phase is cubic structure. The length of the edges of a single Al_3Sc cube is about 10~35 µm. In some cases, there are holes at the centre of the cubic face (Fig. 8c). Similar phenomenon was also reported in [17]. Li *et al* [41] argued that the holes maybe generated by mechanical grinding and polishing. However, the 3D tomography (Fig. 8c) illustrated undoubtedly that such holes were indeed formed during solidification and the explanation is as below. In the solidification process, after an Al_3Sc phase was nucleated and grew into a small cubic shape, new Al_3Sc phases were easily nucleated at the corners or edges of the already formed Al_3Sc cube. Consequently, in the region of the melt in contact with the side surface of the cube, the Sc solute concentration was lower, forming a Sc solute depleted region around the central region of the side surface of the cube, which is, of course, an Al rich region in the centre. When the Sc solute cannot sufficiently migrate laterally towards the centre of the side surface, the holes are formed [17, 42]. Tomography provides rich data for us to quantify the characteristics of the Al_3Sc phases in 3D. Fig. 8d shows that the volumes of the Al_3Sc clusters are in the range of 5000-80000 $µm^3$ with a peak value at 10000 $µm^3$. While, the volume of individual Al_3Sc cube (the insert in Fig.8d) is in the range of 1000-4000 $µm^3$ with a relative even distribution. Fig. 8e shows that the volume of primary Al_3Sc phases increased with increasing surface area with a linear relationship of Y = -1098 + 2.5*X.

9

The 3D rendering of the Al$_3$Sc clusters in a volume of 240 μm × 240 μm × 240 μm are presented in Fig. 9. Clearly, mostly Al$_3$Sc phases conglomerated in clusters as also reported in [10-12]. Figs. 9b and c present the mean curvatures and Gaussian curvatures for those Al$_3$Sc phases. Fig. 9d shows the distributions of the mean curvatures and Gaussian curvatures. The peak frequencies (μ) of the mean curvature and Gaussian curvature are 0.06 and 0.14, respectively. The standard deviation (σ) of these particles are 0.06 and 0.14, respectively. More vivid information about the 3D characteristics of the primary Al$_3$Sc clusters in 3D is presented in the supplementary video. The tomography study clearly showed that majority of the Al$_3$Sc cubes were conglomerated together as clusters, and most of the individual Al$_3$Sc cubes were interconnected (clearly demonstrated in the video). Such segregation behaviour will inevitably reduce significantly the effectiveness of Al$_3$Sc phases as Al grain nucleating agents. Hence, effective methods to disperse the primary Al$_3$Sc clusters and distribute the individual Al$_3$Sc phases as uniformly as possible in the Al melt would be highly desirable in order to enhance the grain refinement performance of Al$_3$Sc phases. In this aspect, ultrasound melt processing and pulse magnetic field melt processing technologies have been showed to be much effective [4]. The most recent research and new findings made by the researchers in Mi's group in this field will be reported elsewhere.

4. Conclusion

In this paper, we report that the micro-size α-Al$_2$O$_3$ particles present in an Al-2wt% Sc melt can facilitate the formation of stacking faults at the α-Al$_2$O$_3$/Al$_3$Sc interface, which in turn, promoted the heterogenous nucleation of Al$_3$Sc on the α-Al$_2$O$_3$ particles. SEM and tomography revealed that individual primary Al$_3$Sc phases were simple

cubes with the edge length of 10~35 μm; and majority of them were interconnected to form clusters with the accumulative peak volume of ~10000 μm^3. At the Al side of the interface between the Al matrix and an Al_3Sc cube, the Al_3Sc phases could grow into separated particles with each of a few tens of nanometre in diameter, which was caused by the depletion of Sc when the Al_3Sc cubes were formed.

Acknowledgements

Reference

[1] J.G. Kaufman, E.L. Rooy, Aluminum Alloy Castings: Properties, Processes, and Applications, ASM International, Materials Park, OH, 2004.

[2] M.A. Easton, M. Qian, A. Prasad, D.H. StJohn, Curr. Opin. St. M., Recent advances in grain refinement of light metals and alloys, 20 (2016) 13-24. https://doi.org/10.1016/j.cossms.2015.10.001.

[3] Z.L. Liu, Review of grain refinement of cast metals through inoculation: theories and developments, Metall. Mater. Trans. A 48A (2017) 4755-4776. https://doi.org/10.1007/s11661-017-4275-7.

[4] D.G. Eskin, J. Mi, Solidification Processing of Metallic Alloys Under External Fields, Springer, Cham, 2018.

[5] S. Riva, K.V. Yusenko, N.P. Lavery, D.J. Jarvis, S.G. Brown, The scandium effect in multicomponent alloys, Inter. Mater. Rev. 61 (2016) 1-26. https://doi.org/10.1080/09506608.2015.1137692.

[6] D.G. Eskin, Sc applications in aluminum Alloys: overview of Russian research in the 20th Century, in: O. Martin (Eds.), Light Metals 2018, Springer, Cham, 2018, pp. 1565-1572.

[7] J. Røyset, N. Ryum, Scandium in aluminium alloys, Inter. Mater. Rev. 50 (2005) 19-44. https://doi.org/10.1179/174328005X14311.

[8] T. Dorin, M. Ramajayam, A. Vahid, T. Langan, Aluminium scandium alloys, in: Roger Lumley (Eds.), Fundamentals of Aluminium Metallurgy, Woodhead Publishing, Cambridge, 2018, pp. 439-494.

[9] L.S. Toropova, D.G. Eskin, M.L. Kharakterova, T.V. Dobatkina, Advanced Aluminum Alloys Containing Scandium, Taylor &. Francis, London, 2017.

[10] K.B. Hyde, A.F. Norman, P.B. Prangnell, The effect of cooling rate on the morphology of primary Al_3Sc intermetallic particles in Al-Sc alloys, Acta Mater. 49 (2001) 1327-1337. https://doi.org/10.1016/S1359-6454(01)00050-7.

[11] A.F. Norman, P.B. Prangnell, R.S. Mcewen, The solidification behaviour of dilute aluminium-scandium alloys, Acta Mater. 46 (1998) 5715-5732. https://doi.org/10.1016/S1359-6454(98)00257-2.

[12] S.A. Zhou, Z. Zhang, M. Li, D.J. Pan, H.L. Su, X.D. Du, P. Li, Y.C. Wu, Effect of Sc on microstructure and mechanical properties of as-cast Al-Mg alloys, Mater. Des. 90 (2016) 1077-1084. http://dx.doi.org/10.1016/j.matdes.2015.10.132.

[13] P.W. Voorhees, Alloys: scandium overtakes zirconium, Nat. Mater. 5 (2006) 435-436. https://doi.org/10.1038/nmat1663.

[14] E. Clouet, L. Laé, T. Épicier, W. Lefebvre, M. Nastar, A. Deschamps, Complex precipitation pathways in multicomponent alloys, Nat. Mater., 5 (2006) 482-488. https://doi.org/10.1038/nmat1652.

[15] T. Dorina, M. Ramajayam, J. Lamb, T. Langan, Effect of Sc and Zr additions on the microstructure/strength of Al-Cu binary alloys, Mater. Sci. Eng. A 707 (2017) 58-64. http://doi.org/10.1016/j.msea.2017.09.032.

[16] Y. Buranova, V. Kulitskiy, M. Peterlechner, A. Mogucheva, R. Kaibyshev,
S.V. Divinski, G. Wilde, $Al_3(Sc,Zr)$-based precipitates in Al-Mg alloy: Effect of severe deformation, Acta Mater. 124 (2017) 210-224.
http://doi.org/10.1016/j.actamat.2016.10.064.

[17] J.H. Li, B. Oberdorfer, S. Wurster, P. Schumacher, Impurity effects on the nucleation and growth of primary Al$_3$(Sc,Zr) phase in Al alloys, J. Mater. Sci. 49 (2014) 5961-5977. https://doi.org/10.1007/s10853-014-8315-z.

[18] Y.J. Shi, Q.L. Pan, M.J. Li, X. Huang, B. Li, Influence of alloyed Sc and Zr, and heat treatment on microstructures and stress corrosion cracking of Al-Zn-Mg-Cu alloys, Mater. Sci. Eng. A 621 (2015) 173-181.

https://doi.org/10.1016/j.msea.2014.10.058.

[19] C. Xu, R. Du, X.J. Wang, S. Hanada, H. Yamagata, W.H. Wang, Effect of cooling rate on morphology of primary particles in Al-Sc-Zr master alloy, T. Nonferr. Metals Soc. 24 (2014) 2420-2426. https://doi.org/10.1016/S1003-6326(14)63366-5.

[20] F. Chen, F. Mao, Z.N. Chen, J.Y. Han, G.Y. Yan, T.M. Wang, Z.Q. Cao, Application of synchrotron radiation X-ray computed tomography to investigate the agglomerating behavior of TiB$_2$ particles in aluminium, J. Alloys Comp. 622 (2015) 831-836. https://doi.org/10.1016/j.jallcom.2014.10.190.

[21] J. Kastner, B. Harrer, H.P. Degischer, High resolution cone beam X-ray computed tomography of 3D-microstructures of cast Al-alloys, Mater. Character. 62 (2011) 99-107. https://doi.org/10.1016/j.matchar.2010.11.004.

[22] P. Pietsch, V. Wood, X-Ray tomography for lithium ion battery research: a practical guide, Annu. Rev. Mater. Res., 47 (2017) 451-479. https://doi.org/10.1146/annurev-matsci-070616-123957.

[23] W. Zhang, B. Lin, Z. Luo, Y. Zhao, Y. Li, Formation of Fe-rich intermetallic compounds and their effect on the tensile properties of squeeze-cast Al-Cu alloys, J. Mater. Res. 30 (2015) 2474-2484. https://doi.org/10.1557/jmr.2015.215.

[24] Y. Zhao, W. Du, B. Koe, T. Connolley, S. Irvine, P.K. Allan, C.M. Schlepütz, W. Zhang, F. Wang, D.G. Eskin, J. Mi, 3D characterisation of the Fe-rich intermetallic phases in recycled Al alloys by synchrotron X-ray microtomography and skeletonisation, Scr. Mater. 146 (2018) 321-326. https://doi.org/10.1016/j.scriptamat.2017.12.010.

[25] Y.L. Zhao, Z. Wang, C. Zhang, W.W. Zhang, Synchrotron X-ray tomography investigation of 3D morphologies of intermetallic phases and pores and their effect on the mechanical properties of cast Al-Cu alloys, J. Alloy. Compd. 777 (2019) 1054-1065. https://doi.org/10.1016/j.jallcom.2018.10.334.

[26] Y.L. Zhao, D.F. Song, B. Lin, C. Zhang, D.H. Zheng, S. Inguva, T. Li, Z.Z Sun, Z. Wang, W.W. Zhang, 3D characterization of ultrasonic melt processing on the

13

microstructural refinement of Al-Cu alloys using synchrotron X-ray tomography, Mater. Charact. 153 (2019) 354-365. https://doi.org/10.1016/j.matchar.2019.04.040.

[27] Y.L. Zhao, B. Lin, D.F. Song, D.H. Zheng, Z.Z. Sun, C.X. Xie, W.W. Zhang, Effect of compound fields of ultrasonic vibration and applied pressure on the 3D microstructure and tensile properties of recycled Al-Cu-Mn-Fe-Si alloys, Materials 12 (2019) 3904. https://doi:10.3390/ma12233904.

[28] A. Mirone, E. Brun, E. Gouillart, P. Tafforeau, J. Kieffer, The PyHST2 hybrid distributed code for high speed tomographic reconstruction with iterative reconstruction and a priori knowledge capabilities, Nucl. Instrum. Meth. B 324 (2014) 41-48. http://dx.doi.org/10.1016/j.nimb.2013.09.030.

[29] C.A. Schneider, W.S. Rasband, K.W. Eliceiri, NIH Image to ImageJ: 25 years of image analysis, Nat. Methods 9 (2012) 671–675. https://doi.org/10.1038/nmeth.2089.

[30] Thermo Scientific Avizo Software 9 User's Guide, Thermo Fisher Scientific, 2018. https://www.fei.com/WorkArea/DownloadAsset.aspx?id=34359741225.

[31] R. Mendoza, J. Alkemper, P.W. Voorhees, The morphological evolution of dendritic microstructures during coarsening, Metall. Mater. Trans. A 34 (2003) 481-489. https://doi.org/10.1007/s11661-003-0084-2.

[32] J. Wang, Z.P. Guo, S. M. Xiong, Characterization of the morphology of primary silicon particles using synchrotron X-ray tomography, Mater. Charact. 123 (2017) 354-359. https://doi.org/10.1016/j.matchar.2016.12.004

[33] J.L. Murray, The Al-Sc (aluminum-scandium) system, J. Phase Equilibr. 19 (1998) 380-384. https://doi.org/10.1361/105497198770342120.

[34] M.A. Kerkove, T.D. Wood, P.G. Sanders, S.L. Kampe, D. Swenson, The diffusion coefficient of scandium in dilute aluminum-scandium alloys, Metall. Mater. Trans A 45A (2014) 3800-3805. http://10.1007/s11661-014-2275-4.

[35] B.A. Chen, G. Liu, R.H. Wang, J.Y. Zhang, L. Jiang, J.J. Song, J. Sun, Effect of interfacial solute segregation on ductile fracture of Al-Cu-Sc alloys, Acta Mater. 61 (2013) 1676-1690. http://doi.org/10.1016/j.actamat.2012.11.043.

[36] X. Liu, J.L. Xue, Z.C. Guo, C. Zhang, Segregation behaviors of Sc and unique primary Al_3Sc in Al-Sc alloys prepared by molten salt electrolysis, J. Mater. Sci. Technol. 35 (2019) 1422-1431. https://doi.org/10.1016/j.jmst.2019.02.002.

[37] Z. Wang, K. Georgarakis, K. S. Nakayama, Y. Li, A. A. Tsarkov, G. Xie, D. Dudina, D. V. Louzguine-Luzgin, A. R. Yavari, Microstructure and mechanical

behavior of metallic glass fiber reinforced Al alloy matrix composites, Sci. Rep. 6 (2016) 24384. https://doi.org/10.1038/srep24384.

[38] W. Kurz, D.J. Fisher, Fundamentals of Solidification, Trans. Tech. Publication Ltd. Switzerland, 1998, 27-28.

[39] R.W. Cahn, K. Hono, P. Haasen, Physical Metallurgy, Elsevier Science B.V., Amsterdam, 4th ed, 1996, 1846-1851.

[40] D.A. Porter, K.E. Easterling, M.Y. Sherif, Phase Transformations in Metals and Alloys, CRC Press, FL, 2009.

[41] Y.K. Li, X.D. Du, J.W. Fu, Y. Zhang, Z. Zhang, S.A. Zhou, Y.C. Wu, Modification mechanism and growth process of Al_3(Sc, Zr) Particles in as-cast Al-Si-Mg-Cu-Zr-Sc alloy, Arch. Foundry Eng., 18 (2018) 51-56. https://doi.org/10.24425/122502.

[42] M.C. Fleming, Solidification Processing. McGraw-Hill, London, 1974.
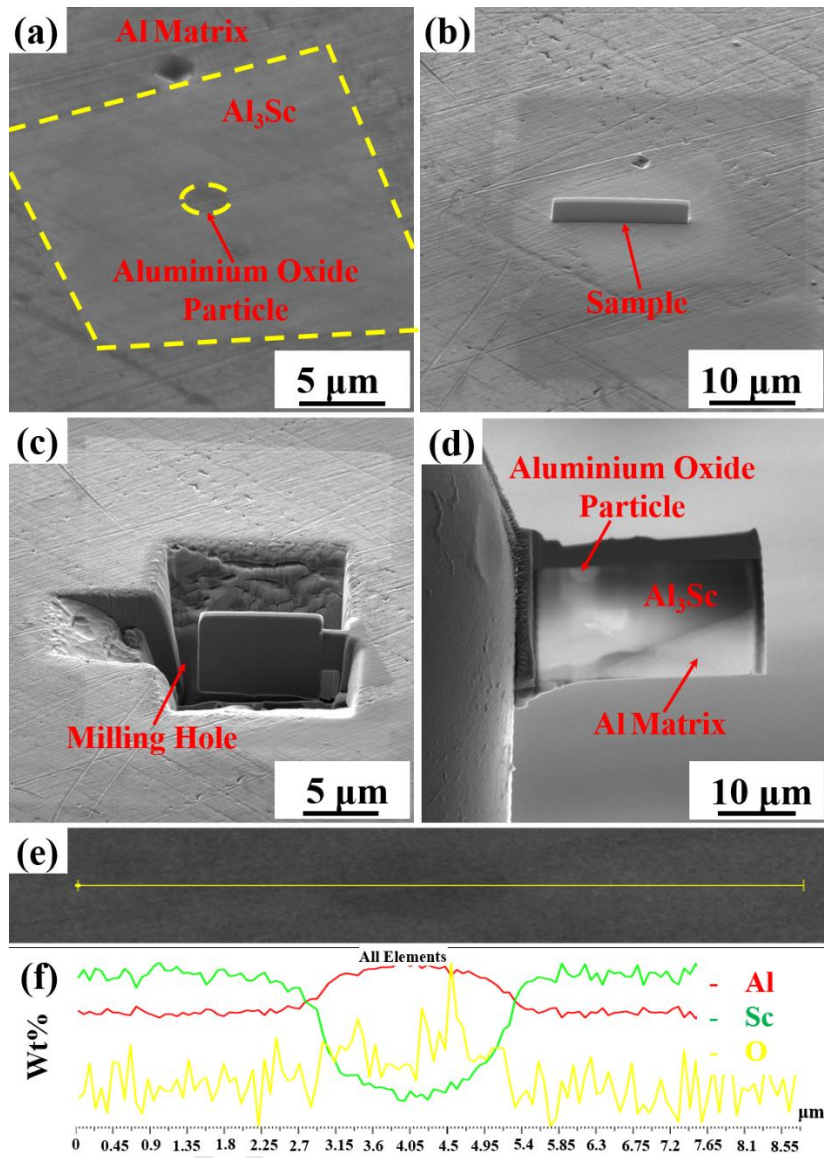
Fig. 1. SEM/FIB images, showing the machining steps used to machine the TEM thin foil sample, and how to identify the possible nucleation site: (a) a SEM image shows an Al₃Sc phase and the surrounding Al matrix; (b) An ion milled thin slice; (c) The milled trench around the thin slice; (d) the thin slice was welded onto a sample holder; (e) and (f) show the EDS line scans for Al, Sc and Oxygen, indicating that the feature in the middle of the Al₃Sc is an aluminium oxide.
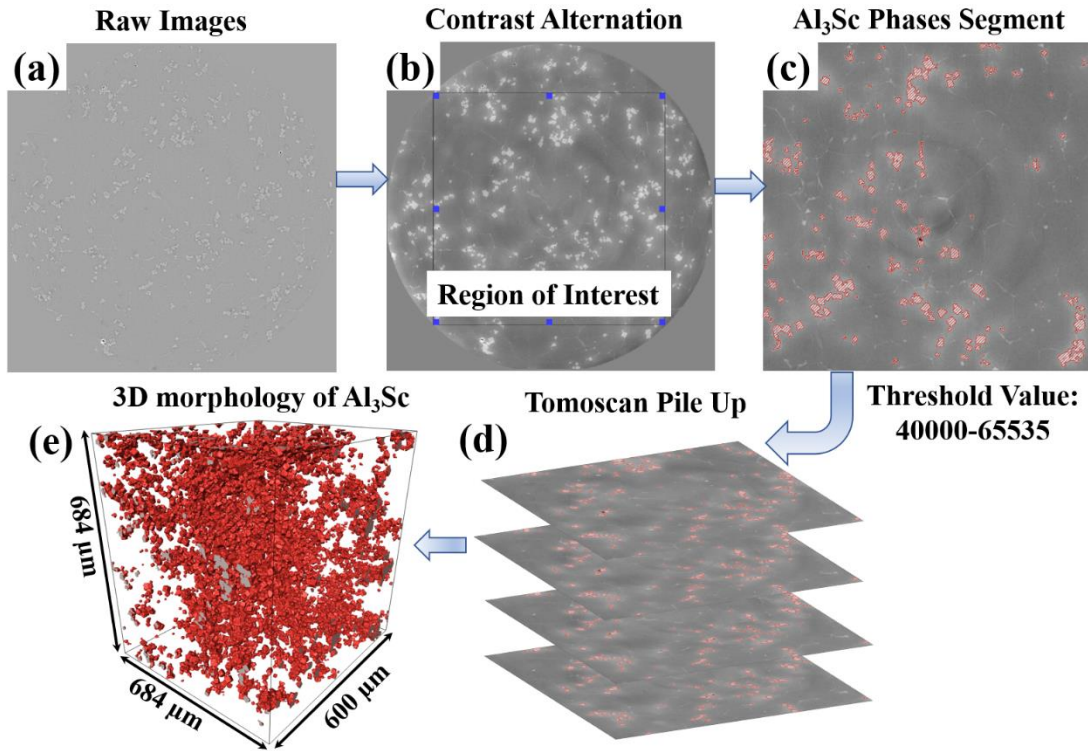
16

Raw Images

(a)

Contrast Alternation

(b)

Region of Interest

Al₃Sc Phases Segment

(c)

3D morphology of Al₃Sc

(e)

684 μm

684 μm

600 μm

Tomoscan Pile Up

(d)

Threshold Value:
40000-65535

Fig. 2. Image processing procedure for the primary Al$_3$Sc phases: (a) a raw X-ray projection; (b) selection of the region of interest, and enhancement of contrast using ImageJ; (c) segmentation of the primary Al$_3$Sc phases according to a predefined grey level threshold; (d) volume rendering of the Al$_3$Sc phases using Avizo; (e) 3D reconstruction of the segmented Al$_3$Sc phases.
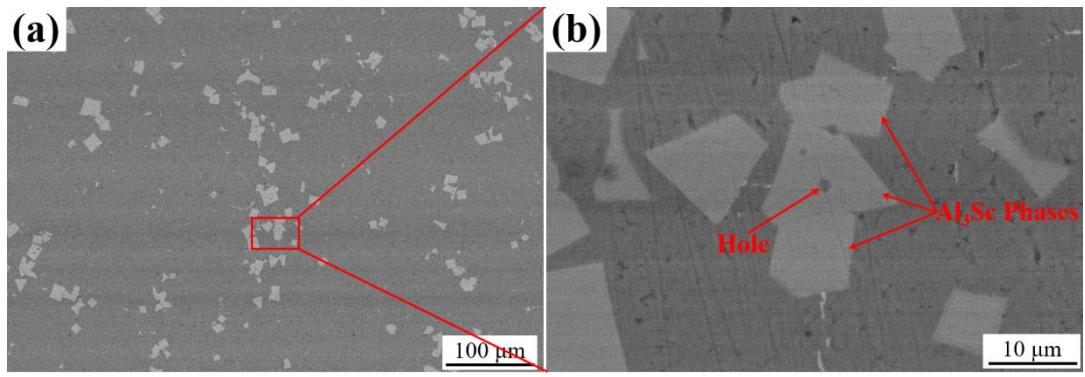
Fig. 3. (a) A typical SEM image, showing the primary Al$_3$Sc phases; (b) an enlarged image of the Al$_3$Sc phases.
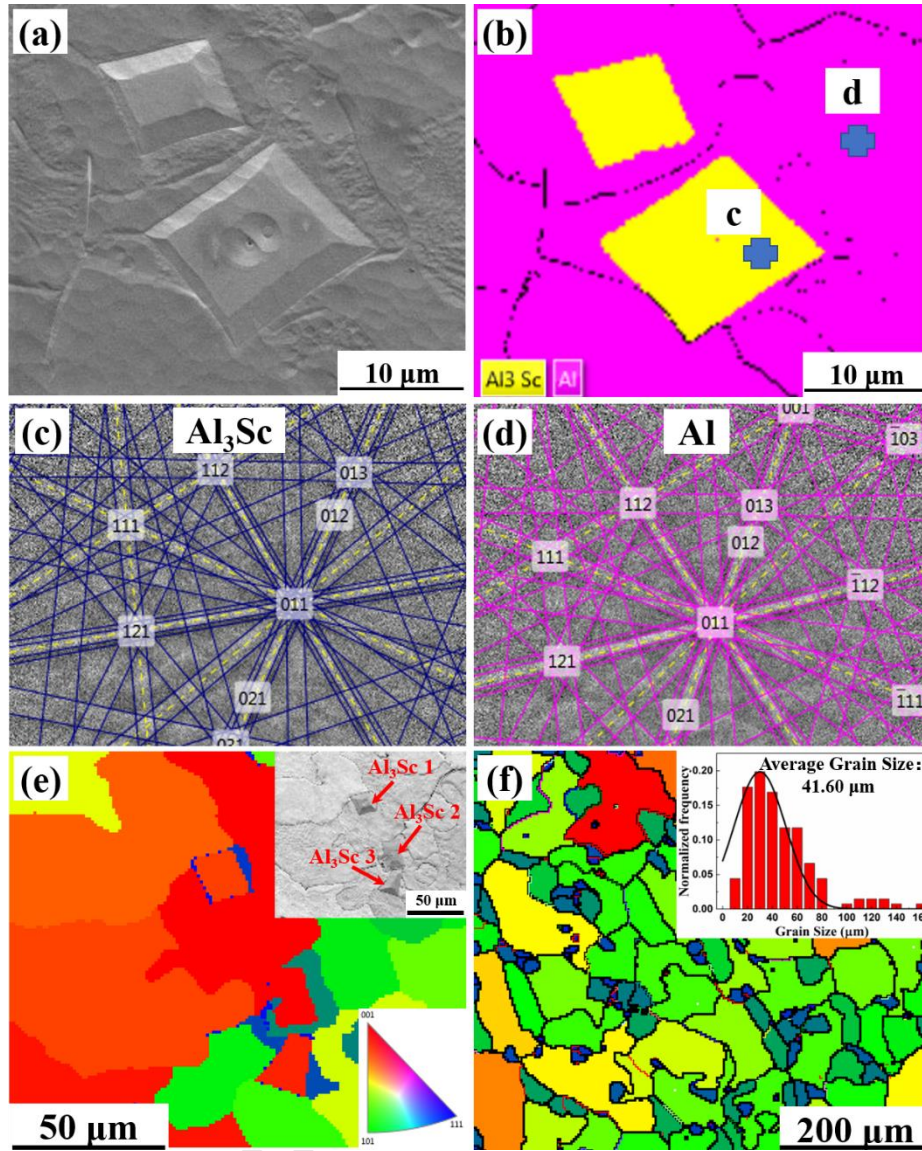
Fig. 4. EBSD analysis of the Al₃Sc phases: (a) a SEM image; (b) a colour-coded image by using the True Phase model, showing the Al matrix (pink) and the Al₃Sc phases (yellow); (c) the Kikuchi patterns of the Al₃Sc phases, and (d) that of the Al matrix; (e) The inverse pole figure, showing the same crystal orientation between three Al₃Sc phases (more clearly in the inserted SEM image) and the Al grains around them; (f) An EBSD orientation map, showing the α-Al grains and their size distribution (the insert).
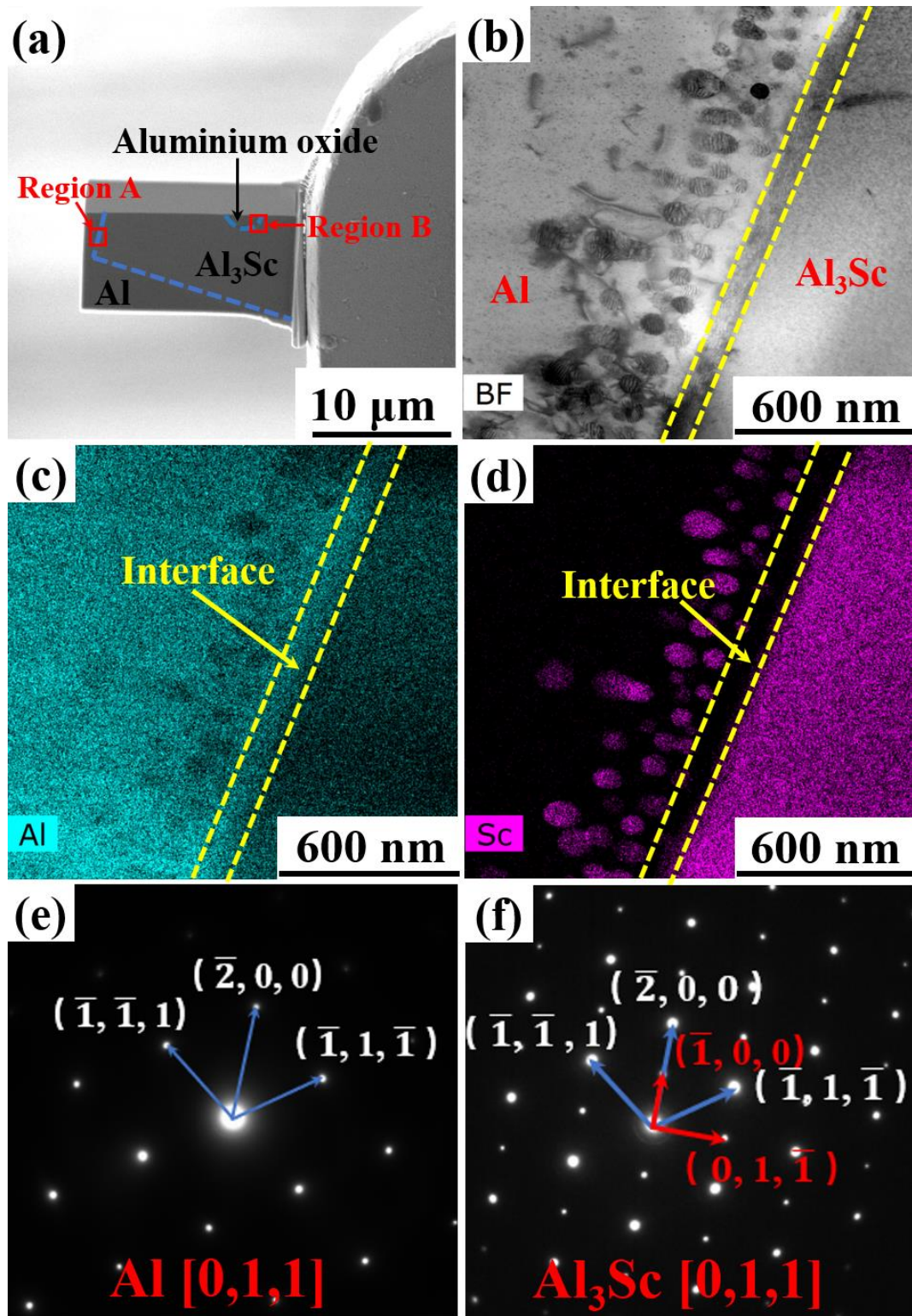
Fig. 5. (a) The FIB machined thin foil that contains an aluminium oxide, Al₃Sc phase and Al matrix; (b) A TEM image of the interface between an Al matrix and Al₃Sc phases; (c) and (d) EDS element mapping of the Al-Al₃Sc interface showed in region A of Fig. 5(b). The SADPs of (e) Al matrix, and (f) Al₃Sc phases.
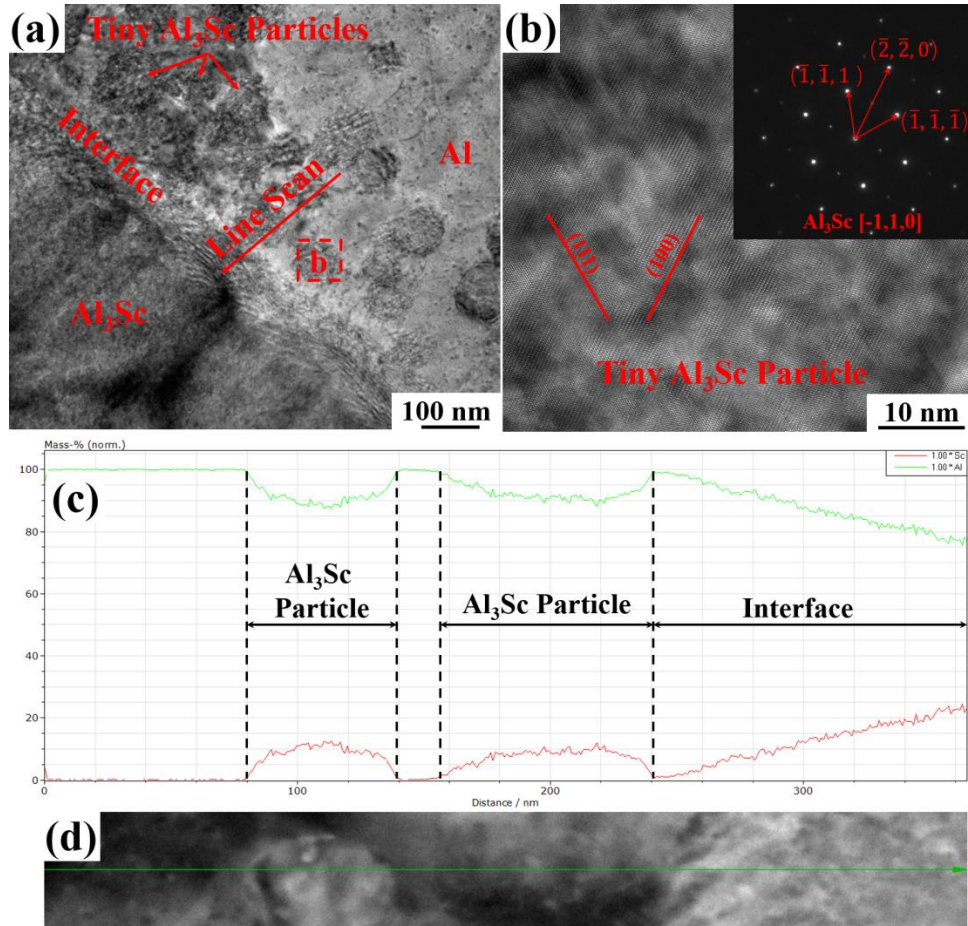
Fig. 6. (a) The enlarged Al-Al$_3$Sc interface in Fig. 5b; (b) A high resolution TEM image of the tiny Al$_3$Sc particle, inserted image showing the SDAP of Al$_3$Sc particle; (c-d) Line scanning across the Al-Al$_3$Sc interface showing the variation of Sc concentration along the line.

21
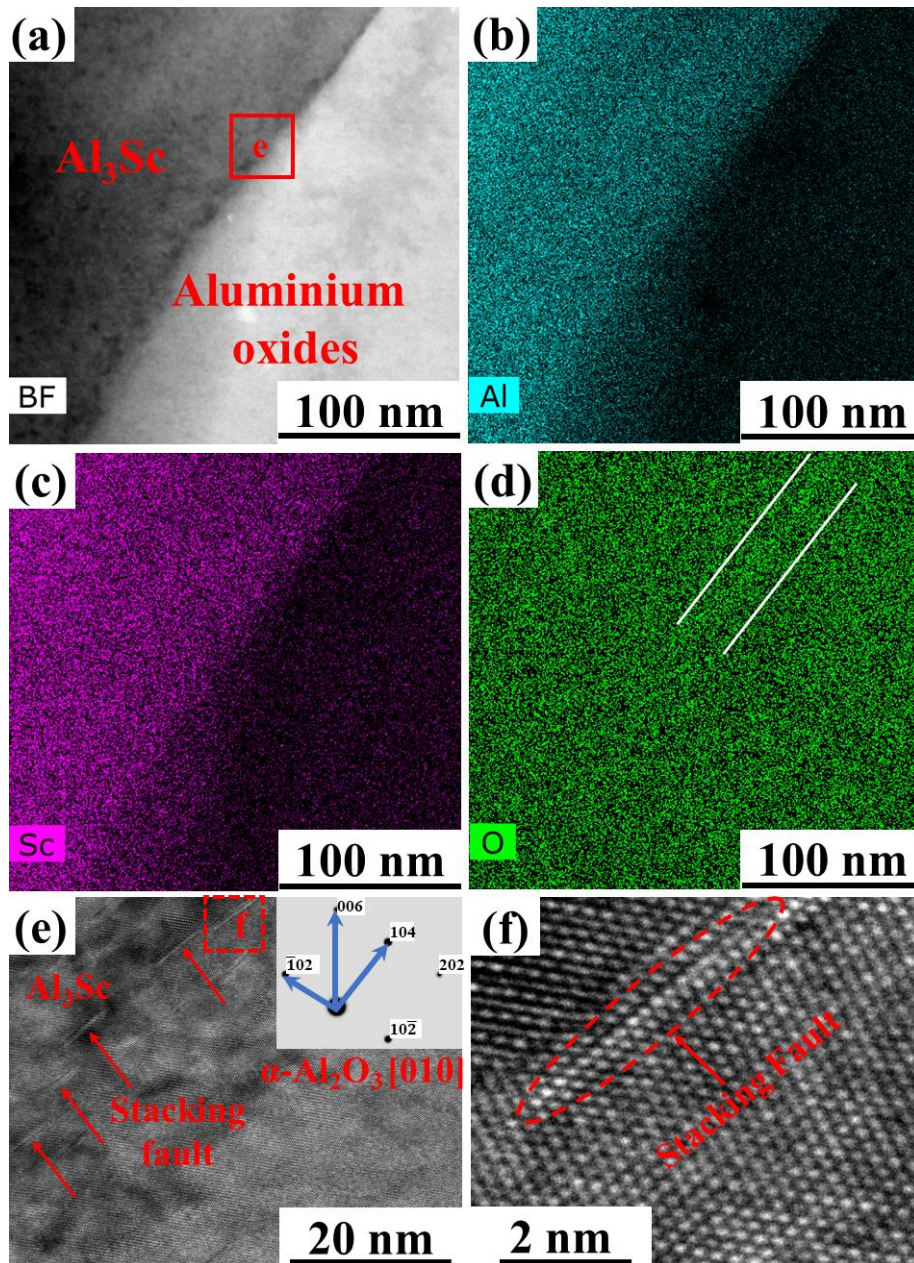
Fig. 7 (a) A TEM bright field image, showing the interface between an Al$_3$Sc phase and an α-Al$_2$O$_3$. EDS elemental maps for (b) Al, (c) Sc and (d) O across the interface; (e) stacking faults found on the Al$_3$Sc phase, an inserted image shows the SDAP of the α-Al$_2$O$_3$; (f) a high-resolution TEM image, showing the stacking fault in Fig. 6e marked by dash red rectangle.
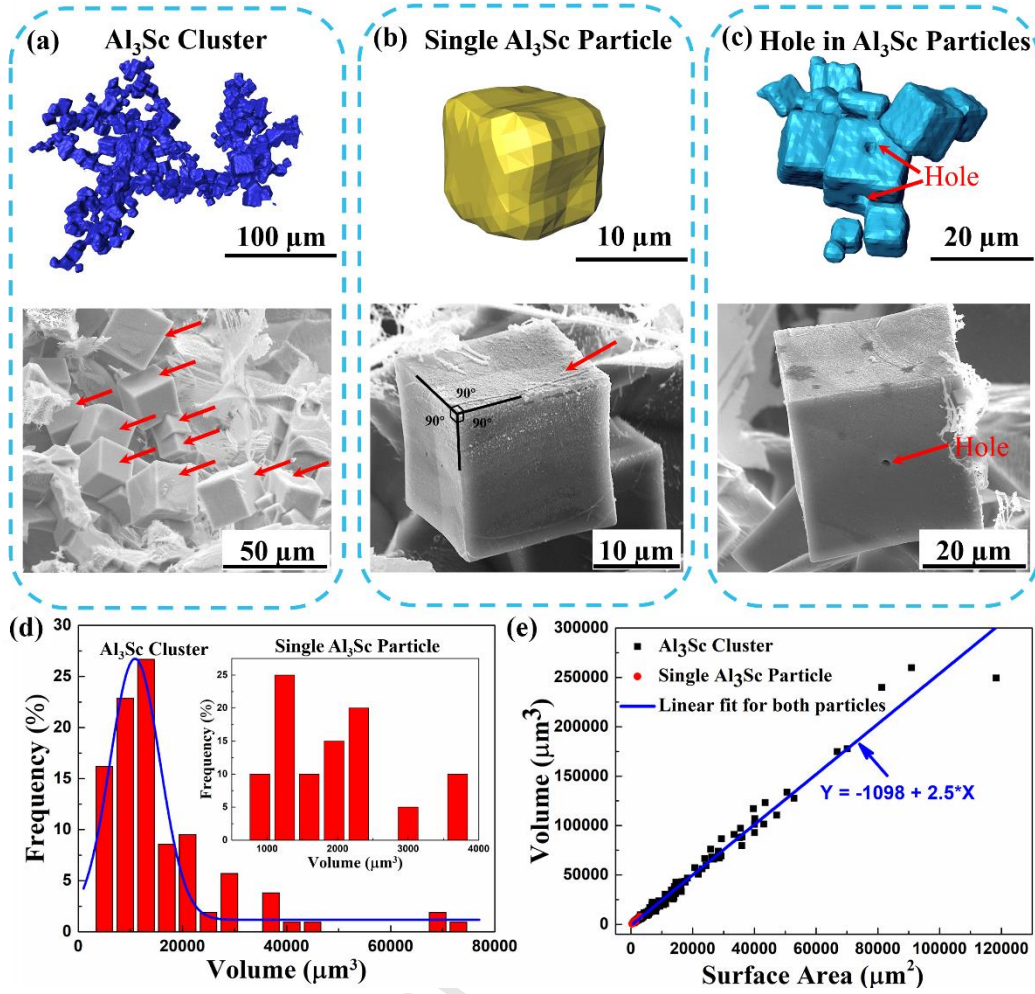
Fig. 8. 3D morphologies of the primary Al$_3$Sc phases: (a) primary Al$_3$Sc clusters; (b) a single primary Al$_3$Sc cube; (c) holes in the Al$_3$Sc cubes; (d) volume distribution of Al$_3$Sc clusters (insert graph: for individual Al$_3$Sc cube); (e) the surface area of Al$_3$Sc particles as a function of volume.
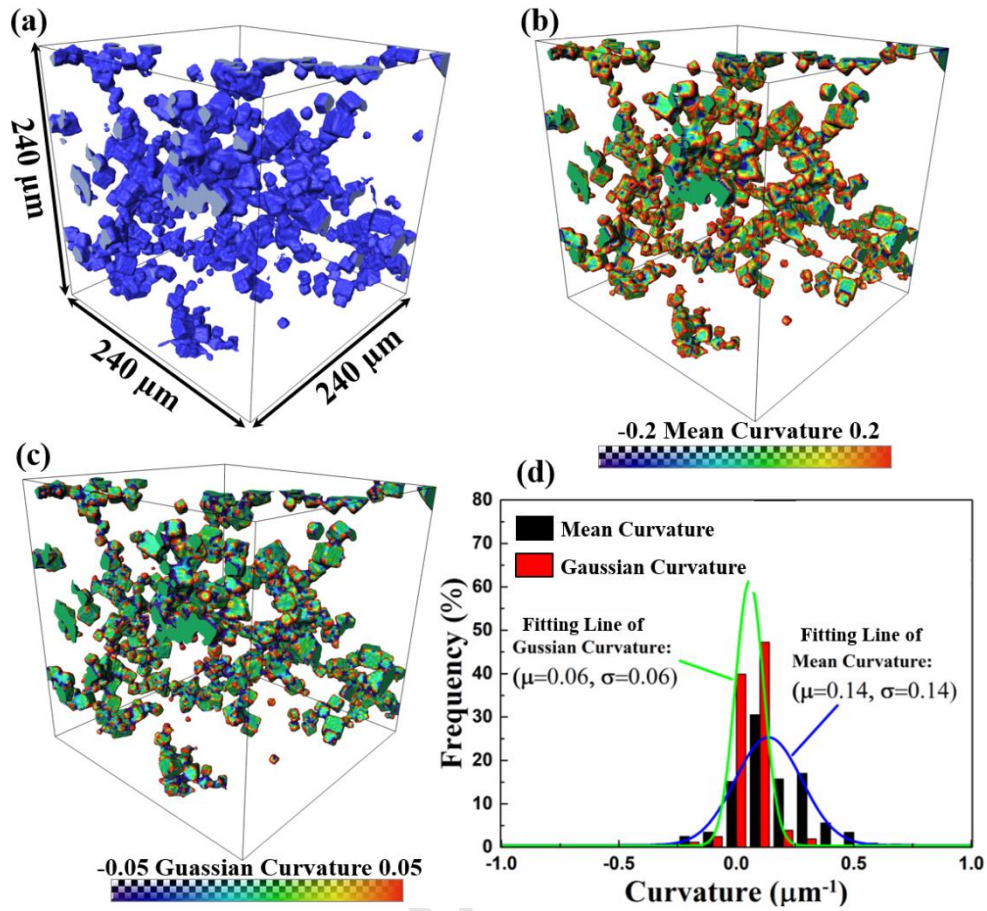
Fig. 9. 3D characterization of the primary Al$_3$Sc phases in a volume of 240 μm × 240 μm × 240 μm: (a) 3D reconstructed Al$_3$Sc cube clusters; (b) the mean curvatures, and (c) Gaussian curvatures for those cubes; (d) distributions of the mean curvatures and Gaussian curvatures.
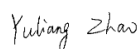
Table 1 The parameters used for the tomography acquisition at ID19, ESRF.

X-ray Beam	Pink beam, 26 keV
Scintillator	LuAG: Ce 25 μm
Detector	PCO. DIMAX
Effective pixel size	1.2 μm
Detector area	1008 × 1008 pixels
Exposure Time	2.0 ms
Magnification	9 ×
No. of Projections	1000
Sample-to-Scintillator distance	300 mm

Author Statement

Due to their contribution to this manuscript (ID: MATERIALSCHAR_2019_3491, Title: Multiscale characterisation of the nucleation and 3D structure of Al_3Sc phases using electron microscopy and synchrotron X-ray tomography), we would like to add Prof. Da Shu and Prof. Baode Sun from Shanghai Jiaotong University, China, as the co-authors. The reason is as following: (1) assisting the TEM sample preparation, analysis and interpretation during the manuscript revision; (2) providing the experimental materials. All the co-authors are agreed to add Prof. Da Shu and Prof. Baode Sun as the co-authors, the signs are shown as following:
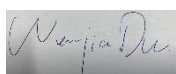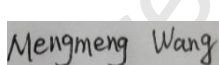
Yuliang Zhao

Weiwen Zhang

Billy Koe

Wenjia Du

Mengmeng Wang

Weilin Wang

Elodie Boller

Alexander Rack

Zhenzhong Sun

Jiawei Mi

Conflict of Interest

The authors declare that there is no conflict of interest.

Highlights

• 3D cubes and cluster Al_3Sc particles are obtained by synchrotron X-ray tomography.

• $\alpha\text{-}Al_2O_3$ is the possible nucleation sites for primary Al_3Sc particles.

• Tiny Al_3Sc particles are formed at Al/Al_3Sc interface due to solute diffusion.

• Stacking faults at $\alpha\text{-}Al_2O_3/Al_3Sc$ interface promote heterogenous nucleation of Al_3Sc.